1   **A quantitative map of nuclear pore assembly reveals two distinct mechanisms**

2

3   Shotaro Otsuka[1,3]*, Jeremy O. B. Tempkin[2], Antonio Z. Politi[1,4], Arina Rybina[1], M. Julius

4   Hossain[1], Moritz Kueblbeck[1], Andrea Callegari[1], Birgit Koch[1,5], Andrej Sali[2] and Jan Ellenberg[1]*

5

6   [1]Cell Biology and Biophysics Unit, European Molecular Biology Laboratory, Meyerhofstrasse 1,

7   69117 Heidelberg, Germany.

8   [2]Department of Bioengineering and Therapeutic Sciences, Department of Pharmaceutical

9   Chemistry, Quantitative Biosciences Institute, University of California, San Francisco, San

10   Francisco, CA 94143, USA.

11   [3]Present address: Max Perutz Labs, a joint venture of the University of Vienna and the Medical

12   University of Vienna, Vienna Biocenter (VBC), Dr. Bohr Gasse 9, 1030 Vienna, Austria.

13   [4]Present address: Max Planck Institute for Biophysical Chemistry, Göttingen, Germany.

14   [5]Present address: Max Planck Institute for Medical Research, Heidelberg, Germany

15   *Correspondence: shotaro.otsuka@univie.ac.at; jan.ellenberg@embl.de

16

17   **Summary**

18   Understanding how the nuclear pore complex (NPC) assembles is of fundamental importance to

19   grasp the mechanisms behind its essential function and understand its role during evolution of

20   eukaryotes[1–4]. While we know that at least two NPC assembly pathways exist, one during exit

21   from mitosis and one during nuclear growth in interphase, we currently lack a quantitative map of

22   their molecular events. Here, we use fluorescence correlation spectroscopy (FCS) calibrated live

23   imaging of endogenously fluorescently-tagged nucleoporins to map the changes in composition

24   and stoichiometry of seven major modules of the human NPC during its assembly in single

25   dividing cells. This systematic quantitative map reveals that the two assembly pathways employ

26   strikingly different molecular mechanisms, inverting the order of addition of two large structural

27   components, the central ring complex and nuclear filaments. Our dynamic stoichiometry data

28   allows us to perform the first computational simulation that predicts the structure of postmitotic

29   NPC assembly intermediates.

30

31   The nuclear pore complex (NPC) is the largest non-polymeric protein complex in eukaryotic cells.

32   It spans the double membrane of the nucleus (nuclear envelope; NE) to mediate the

33   macromolecular transport between the nucleus and the cytoplasm. To achieve this essential

34   function, the NPC forms an octameric proteinaceous channel composed of multiples of eight of

35   over 30 different nucleoporins (Nups) that form 6–8 protein modules, the NPC subcomplexes[1,2].

36   Therefore, more than 500 individual proteins have to come together to assemble one nuclear pore,

37   which has the mass of tens of ribosomes. NPCs are thought to represent a key step in the evolution

38   of endomembrane compartmentalization that allowed ancestral eukaryotes to separate their

39   genome from the cytoplasm[3,4].

40   In proliferating cells, there are two main pathways to assemble the NPCs. During nuclear

41   assembly after mitosis, the NPCs form together with nuclear membranes to rapidly build new

42   nuclei in the daughter cells (called postmitotic NPC assembly). During nuclear growth in

43   interphase, NPCs then continue to assemble continuously for homeostasis (referred to as

44   interphase assembly). Research over the last decade has revealed that postmitotic and interphase

45   NPC assembly possess distinct kinetic, molecular and structural features[5–12], suggesting that two

46   fundamentally different mechanisms build the same protein complex. In postmitotic assembly,

47   several thousand NPCs assemble within a few minutes during sealing of the initially fenestrated

48   nuclear membranes, whereas interphase NPC assembly occurs more sporadically, requires about

49   one hour, and involves a new discontinuity in the double membrane barrier of the NE. Studies

50   using molecular depletions have shown that the Nup ELYS is required for postmitotic assembly

2

51   but appears dispensable for interphase assembly[5], whereas the membrane curvature-sensing

52   domain of Nup133[6], Pom121 and Sun1[7,8], the import of Nup153 into the nucleus[9], and Torsins[10]

53   seem to be required only for interphase assembly. Recent studies correlating real time imaging

54   with three-dimensional electron microscopy have revealed that postmitotic NPC assembly

55   proceeds by radial dilation of small membrane openings[11], while in interphase, assembly induces

56   an asymmetric inside-out fusion of the inner and outer nuclear membranes[12].

57   However, how several hundred proteins self-organize to form the NPC channel *via* these two

58   distinct assembly pathways has remained largely enigmatic. It is technically challenging to locate

59   the transient and rare assembly events, which has prevented investigation of the structure of

60   assembly intermediates by either cryo-EM tomography or super-resolution microscopy. In

61   addition, the large number of building blocks and their cooperativity often leads to complex

62   nonlinear kinetics that can only be interpreted mechanistically using computational modelling of

63   the structures formed during assembly. While we have some information about the dynamic

64   addition of Nups after mitosis[13,14], only sparse dynamic data is available for interphase

65   assembly[15,16]. Importantly, these earlier studies could not distinguish postmitotic and interphase

66   assemblies, whose co-occurrence in different regions of the nucleus was only discovered later;

67   moreover, these studies provided only qualitative descriptions as they relied on ectopic expression

68   of fluorescently-tagged Nups. Kinetic data about NPC assembly that can distinguish between the

69   postmitotic and interphase pathways is required, including the copy numbers of Nups that

70   assemble into forming NPCs over time. Such data would enable modeling of the assembly process

71   and allow us to start to understand the two assembly mechanisms.

72

73   **Quantitative live imaging of ten nucleoporins representing seven major NPC building blocks**

74   To quantitatively analyze the changes in concentration of Nups at the NE during exit from mitosis

75   and nuclear growth in G1, we genome-edited HeLa cells, homozygously tagging the endogenous

76   genes for ten different Nups with mEGFP or mCherry. We chose proteins that represent the major

77   building blocks of the fully assembled pore, including the nuclear filament protein Tpr, the nuclear

78   Nup153, the Y-complex members Nup107 and Seh1, the central ring complex members Nup93

79   and Nup205, the central channel protein Nup62, the transmembrane protein Pom121 as well as the

80   cytoplasmic filament proteins Nup214 and Nup358. Homozygous tagging was verified by careful

81   quality control of the genome edited monoclonal cell lines[17], ensuring that the tagged subunit was

82   expressed at physiological levels, localized to the NPC and that cell viability and mitotic

83   progression were normal (Figs. 1 and 2). The fusion proteins are likely functional, given that most

84   Nups show strong phenotypes upon knock-out or depletion[18].

85   To characterize the fluorescently-tagged Nups, we first performed super-resolution (STED)

86   microscopy to determine NPC density in fully grown nuclei of the knock-in cell lines, showing

87   that homozygous tagging had little effect on NPC density that was comparable within 15%

88   between all cell lines with an average of 10.1 NPC per μm^2 (Fig. 1b, c), in good agreement with

89   our previous estimates by electron microscopy of HeLa cells[12]. We then used fluorescence

90   correlation spectroscopy (FCS) calibrated confocal microscopy[19,20] to determine the concentration

91   and total number of the Nups at the NE in living cells (Extended Data Table 1, for details see

92   Methods). Using the measured NPC density and the Nup concentration at the NE, we could

93   calculate the average copy number of each Nup per NPC (Fig. 1d). This data showed that the

94   investigated Nups were on average present in 16, 32, or 48 copies per pore, as expected from the

95   eightfold symmetry of the complex and overall in good agreement with previous estimates by mass

96   spectrometry[21]. This observation quantitatively validated that the homozygous tagging did not

97   affect the incorporation of the Nups into the NPC. For Nup153 and Pom121 that exhibited lower

98   concentrations likely due to subhomozygous tagging (Fig. 2a, Extended Data Fig. 1), we

99   normalized their stoichiometry to the expected number of copies in the mature pore for comparison

100   (Fig. 3a).

101

NPC assembly relies on and consumes almost half of the material inherited from the mother cell within one hour after mitosis

We then used our validated cell line resource to quantitatively image the Nups during both postmitotic and interphase NPC assembly, from metaphase until the end of the rapid nuclear growth phase in G1, two hours after anaphase onset. To this end, we performed systematic FCS-calibrated 3D confocal time-lapse microscopy[22] (Fig. 2a). Using the single molecule fluctuation calibration, the 4D imaging data could be converted into maps of subcellular protein concentration (Fig. 2a). Counterstaining live nuclei with SiR-DNA[23], enabled computational image segmentation to measure the soluble cytoplasmic pool and the NE associated pool over time[22]. Temporal alignment to anaphase onset then allowed us to compare the dynamic association of all Nups with the NE over time (Fig. 2a). Overall, the investigated Nups are present in 250,000 to 1,200,000 copies per human metaphase cell. After mitosis, this building material is split between the daughter cells with little detectable new protein synthesis in the first hour after anaphase onset (Fig. 2b). Notably, 34–53% of the soluble pool present in the cytoplasm in metaphase was rapidly re-localized to the NE during the first hour after exit from mitosis (43, 38, 47, 37, 41, 44, 53, and 34% for Nup107, Seh1, Nups205, 93, 62, 214, Tpr and Nup358, respectively) (Fig. 2b), indicating that NPC assembly initially relies almost entirely on the pool of building blocks inherited from the mother cell to form the first 4,000–5,000 NPCs[11,12].

Quantitative analysis of multimolecular kinetics of postmitotic and interphase NPC assembly

As we and others have demonstrated previously[12,24], postmitotic and interphase NPC assembly can be observed in the same living cell in different regions of the NE within the first two hours after mitosis. While postmitotic assembly dominates the peripheral "non-core" regions of the NE, the

126   central "inner core" area is only populated with NPCs after exit from mitosis when dense spindle

127   microtubules have been removed from the DNA surface[25]. Using computational segmentation and

128   assignment of the inner-core and non-core regions (Extended Data Fig. 2a), we measured the

129   concentration changes of the ten Nups in these two regions separately. A two-component model

130   of a fast (postmitotic) and a slow (interphase) assembly process fits the experimental data well,

131   allowing us to kinetically unmix the two assembly processes for each Nup (Extended Data Figs.

132   2b–d and 3). In this way, we could for the first time perform an integrated analysis of the real time

133   kinetics of absolute concentration changes of Nups in all major NPC modules during the two

134   assembly processes at the NE (Fig. 3a). This analysis immediately revealed that the overall

135   duration of the two processes is very different, with postmitotic assembly essentially complete 15

136   min after anaphase onset, while interphase assembly only reaches a plateau after 100 min,

137   consistent with our previous estimates based on live cell imaging[13,16] and correlative electron

138   microscopy[11,12]. Both processes reached the same final ratios between the different Nups and thus

139   presumably formed identical NPCs. However, the temporal order in which components were

140   added was distinct, including, for example, an earlier assembly of Pom121 relative to the Y-shaped

141   complex during interphase assembly, consistent with our previous observations[16].

142   To comprehensively investigate the molecular differences between the two assembly

143   processes, we relied on the constant NPC density and changes in nuclear surface area[12] to convert

144   the NE concentrations of all investigated Nups into their average copy number per assembling

145   NPC over time (Fig. 3a). This result in turn enabled us to estimate changes in subunit stoichiometry

146   of the complex during its assembly in living cells. To facilitate the comparative analysis of the

147   assembly kinetics between the two pathways, in which ten components assemble with different

148   speed and order, we first reduced the dimensionality of the kinetic data. To this end, we assigned

149   a single characteristic time-point of assembly to each Nup, by sigmoidal fitting of its full kinetic

150   signature (Extended Data Fig. 4a). Plotting the copy number *vs* the average time-point of assembly

6

151   provides an overview of the major molecular differences between the two assembly pathways (Fig.

152   3b).

153   While the Y-complex, Pom121, and Nup153 form a core of the first modules that assemble

154   almost simultaneously within one minute in postmitotic assembly, these components are stretched

155   out into a clear temporal order of first Nup153, second Pom121, and third the Y-complex (notably

156   with its two investigated subunits also assembling simultaneously in interphase) over more than

157   ten minutes in interphase assembly. The end of assembly on the other hand is marked for both

158   process by the addition of the large cytoplasmic filament protein Nup358. The major difference

159   was thus neither in initiation nor termination of assembly, but rather in the middle of the two

160   assembly pathways. During postmitotic assembly, the Y-complex is rapidly combined with

161   components of the central ring, building the inner core of the pore within only three minutes prior

162   to addition of either cytoplasmic or nuclear filament proteins, which follow later. In contrast,

163   during interphase assembly, the Y-complex is first combined with the nuclear filament protein Tpr

164   and the base of the cytoplasmic filament Nup214, while the central ring complex is added later.

165   This observation clearly shows that postmitotic and interphase NPC assembly not only proceed

166   with different speed but also follow a different molecular mechanism using an inverted molecular

167   order between the central ring and nuclear filaments (Fig. 3b, Extended Data Fig. 4b).

168   To obtain additional insight into the assembly mechanism, it is instructive to go beyond

169   examining the temporal order and examine our data for evidence of coupling between different

170   components of the NPC. Theoretically, for a sequential assembly mechanism where late steps

171   depend on early steps, the observed ensemble kinetics of a late binding protein must contain the

172   history of all previous events (see Methods for details). To test this prediction, we examined if one

173   or both of our assembly pathways exhibited a correlation between the average assembly time and

174   duration of the different components. We plotted the time needed for 90% of one protein to

175   accumulate in the population of assembling pores (the assembly duration) *vs* the time when this

176   accumulation is half maximal in the overall process (the average time-point of assembly) for all

177   analysed Nups (Fig. 3c, Extended Data Fig. 4a). Indeed, postmitotic assembly showed a strong

178   positive linear correlation (Fig. 3c), indicating a sequential assembly mechanism, which for

179   example implies that Nup62 is incorporated into the NPC before Tpr can bind. In contrast,

180   interphase assembly shows poor correlation between duration and time-point of assembly (Fig.

181   3c), indicating a less strictly sequential pathway, where proteins may assemble more

182   independently of each other.

183

184   **Integrative modeling of the NPC assembly pathway**

185   To obtain a more comprehensive mechanistic view, we computed a spatiotemporal model of the

186   macromolecular assembly pathway, based on our dynamic multimolecular stoichiometry data in

187   combination with the available ultrastructural data about NPC assembly[11] and the partial

188   pseudoatomic model of the mature NPC[26,27]. We modeled here only the postmitotic assembly, as

189   it showed the kinetic hallmarks of a sequential process and is known to proceed by dilating an

190   existing membrane pore with a smoothly growing proteinaceous density[11]. We focused on the

191   Nups contained in the structural model of the human NPC, including Nup107 and Seh1 for the Y-

192   complex as well as Nup93, Nup205, and Nup62 for the central ring/channel complex[26,27]. We

193   constrained their copy number by our stoichiometry data for the time points for which correlative

194   electron tomography data is available[11], in order to use the membrane shapes and associated

195   protein densities from the tomography to constrain Nup positions. To structurally model the

196   spatiotemporal assembly process, we generalized our integrative modeling method for determining

197   static structures of macromolecular assemblies[28,29]. In outline (see Methods for details), we first

198   model ensembles of structures at discrete time points, then connect them between time points into

199   assembly trajectories and finally rank the alternative trajectories by fit to our data.

8

200   We focus on the best fitting macromolecular assembly pathway that accounts for over 80% of

201   the posterior model density (the second-scoring accounts for only 19%). This trajectory starts by

202   formation of a single nuclear ring, composed of eight Y-complexes, concomitantly with an initial

203   accumulation of the FG-repeat protein Nup62 and Nup205 in the center of the membrane hole

204   (Fig. 4). The cytoplasmic Y-complex is then added on the cytoplasmic side, before the second set

205   of the Y-complex ring assembles on the nuclear side, again one eight-membered ring after another.

206   In the center of the pore, Nup62 dilates from an amorphous mass into a small ring and associates

207   with Nup205 to form the central ring complex. This "nuclear ring first" assembly mechanism is

208   consistent with the observation of an eight-fold symmetric protein density on the inner nuclear

209   membrane at early stages of assembly[11]. In addition, the early accumulation of Nup62 to the pore

210   center suggests a potential role of the hydrophobic FG-repeats in the initial dilation of the small

211   membrane hole into the larger, NPC sized channel.

212

213   **Discussion**

214   Our data revealed that the two assembly pathways employ strikingly different molecular

215   mechanisms. While it is at first glance surprising that the cell builds the same machine in two

216   fundamentally different ways, these distinct pathways can be rationalized by considering them in

217   the light of the rather different physiological requirements that the cell faces after mitosis and

218   during nuclear growth in interphase. Immediately after exit from mitosis, the nucleus is formed *de*

219   *novo* and the cell needs to rapidly seal its genome, exclude cytoplasm from it[30] and quickly restore

220   import of essential nuclear proteins. Since the new NE originates from highly fenestrated ER

221   sheets, nuclear transport channels can be built without a formal membrane fusion requirement[11].

222   The mechanism we observed for postmitotic assembly, appears well adapted to this context. The

223   rapid assembly of the nuclear Y-ring and the central ring could provide a fast way to prevent

224   complete fusion of the ER membrane holes and assemble a minimal, transport competent

225 proteinaceous phase in them. Assembly of this first "transport core" NPC is complete within less

226 than 10 min after mitosis, which precisely matches the time when transport competence is gained

227 by postmitotic nuclei[13,14].

228 By contrast in telo/G1 phase, the nucleus already has a sealed, double membraned NE with

229 about 2500 postmitotically assembled and transporting pores, but needs to expand to allow the

230 genome to take up its interphase functions. To support nuclear growth, the cell needs to maintain

231 a constant NPC density to ensure sufficient transport capacity and maintain homeostasis to provide

232 enough NPC building blocks for the next cell generation, which we have shown to initially rely

233 completely on material from the mother cell. Interphase NPC assembly requires a *de novo* fusion

234 between the inner and outer nuclear membrane but must not disrupt nuclear integrity. The

235 molecular pathway we observed for interphase assembly makes new predictions about its unique,

236 inside out evaginating, mechanism. The cell first not only builds the two nuclear Y-rings but also

237 accumulates the material for their cytoplasmic counterparts and then combines them with the

238 nuclear filament proteins, all prior to the time of membrane fusion[12]. This mechanism suggests

239 that the cytoplasmic Y-rings, including the base of the cytoplasmic filaments with Nup214, are

240 already "prebuilt" within the inner membrane evagination, where the small available volume

241 would predict that they must be present in a very different structure than in the fully mature pore

242 after fusion. In addition, the unexpectedly early presence of Tpr suggests a key role of this large

243 coiled-coil protein during interphase assembly, potentially in the membrane bending and/or fusion

244 process. Surprisingly, the central ring complex, which is a core structural element between the

245 nuclear and cytoplasmic Y-rings in the mature pore[27] is added only later, suggesting that during

246 interphase assembly, nuclear transport control may only be added after the membrane fusion step.

247 The order of Nup assembly for interphase assembly we observed here is consistent with the

248 recently reported order of NPC assembly in budding yeast that undergoes a closed mitosis[31], except

249 for the Tpr homologues Mlp1/2 which assemble late in yeast[31]. This difference could be due to the

10

250   fundamental differences in cell cycle remodeling of the NE or additional functions of Mlp proteins

251   that are believed to compensate for the absence of lamins in yeast.

252   Beyond the assembly mechanism the two pathways we have mapped here start to shed light

253   on the role of the NPC during evolution of the endomembrane system in eukaryotes[3,4]. We

254   speculate that the modern NPC combines ancient membrane bending (e.g. coiled-coil filaments,

255   such as Tpr) and membrane hole plugging (e.g. FG-repeat proteins of the central ring complex)

256   modules, that were potentially previously used separately for extruding the cell surface or keeping

257   transport channels open in the endomembranes around the genome. The key evolutionary

258   innovation might lie in combining and controlling these activities, potentially by the eight-

259   membered ring architecture of the nuclear Y-complex. In the future, comparing NPC assembly

260   pathways in different species on the eukaryotic evolutionary tree, might help us to understand how

261   the assembly of complex modern protein machines reflects their evolutionary origins.

262

263   **Main references**

264   1   Hampoelz, B., Andres-Pons, A., Kastritis, P. & Beck, M. Structure and Assembly of the

265   Nuclear Pore Complex. *Annu. Rev. Biophys.* **48**, 515–536 (2019).

266   2   Lin, D. H. & Hoelz, A. The Structure of the Nuclear Pore Complex (An Update). *Annu.*

267   *Rev. Biochem.* **88**, 725–783 (2019).

268   3   Baum, D. A. & Baum, B. An inside-out origin for the eukaryotic cell. *BMC Biol.* **12**, 76

269   (2014).

270   4   Otsuka, S. & Ellenberg, J. Mechanisms of nuclear pore complex assembly - two different

271   ways of building one molecular machine. *FEBS lett.* **592**, 475–488 (2018).

272   5   Franz, C. *et al.* MEL-28/ELYS is required for the recruitment of nucleoporins to chromatin

273   and postmitotic nuclear pore complex assembly. *EMBO Rep.* **8**, 165–172 (2007).

274   6   Doucet, C. M., Talamas, J. A. & Hetzer, M. W. Cell cycle-dependent differences in nuclear

275   pore complex assembly in metazoa. *Cell* **141**, 1030–1041 (2010).

276   7   Talamas, J. A. & Hetzer, M. W. POM121 and Sun1 play a role in early steps of interphase

277   NPC assembly. *J. Cell Biol.* **194**, 27–37 (2011).

278   8   Funakoshi, T., Clever, M., Watanabe, A. & Imamoto, N. Localization of Pom121 to the

279   inner nuclear membrane is required for an early step of interphase nuclear pore complex

280   assembly. *Mol. Biol. Cell* **22**, 1058–1069 (2011).

281   9   Vollmer, B. *et al.* Nup153 Recruits the Nup107-160 Complex to the Inner Nuclear

282   Membrane for Interphasic Nuclear Pore Complex Assembly. *Dev. Cell* **33**, 717-728 (2015).

283   10   Rampello, A. J. *et al.* Torsin ATPase deficiency leads to defects in nuclear pore biogenesis

284   and sequestration of MLF2. *J. Cell Biol.* **219** (2020).

285   11   Otsuka, S. *et al.* Postmitotic nuclear pore assembly proceeds by radial dilation of small

286   membrane openings. *Nat. Struct. Mol. Biol.* **25**, 21–28 (2018).

287   12   Otsuka, S. *et al.* Nuclear pore assembly proceeds by an inside-out extrusion of the nuclear

288   envelope. *Elife* **5** (2016).

289   13   Dultz, E. *et al.* Systematic kinetic analysis of mitotic dis- and reassembly of the nuclear

290   pore in living cells. *J. Cell Biol.* **180**, 857–865 (2008).

291   14   Otsuka, S., Szymborska, A. & Ellenberg, J. Imaging the assembly, structure, and function

292   of the nuclear pore inside cells. *Methods Cell Biol.* **122**, 219–238 (2014).

293   15   D'Angelo, M. A., Anderson, D. J., Richard, E. & Hetzer, M. W. Nuclear pores form de

294   novo from both sides of the nuclear envelope. *Science* **312**, 440–443 (2006).

295   16   Dultz, E. & Ellenberg, J. Live imaging of single nuclear pores reveals unique assembly

296   kinetics and mechanism in interphase. *J. Cell Biol.* **191**, 15–22 (2010).

297   17   Koch, B. *et al.* Generation and validation of homozygous fluorescent knock-in cells using

298   CRISPR-Cas9 genome editing. *Nat. Protoc.* **13**, 1465–1487 (2018).

299   18   Guglielmi, V., Sakuma, S. & D'Angelo, M. A. Nuclear pore complexes in development
300   and tissue homeostasis. *Development* **147** (2020).

301   19   Wachsmuth, M. *et al.* High-throughput fluorescence correlation spectroscopy enables
302   analysis of proteome dynamics in living cells. *Nat. Biotechnol.* **33**, 384–389 (2015).

303   20   Politi, A. Z. *et al.* Quantitative mapping of fluorescently tagged cellular proteins using
304   FCS-calibrated four-dimensional imaging. *Nat. Protoc.* **13**, 1445–1464 (2018).

305   21   Ori, A. *et al.* Cell type-specific nuclear pores: a case in point for context-dependent
306   stoichiometry of molecular machines. *Mol. Syst. Biol.* **9**, 648 (2013).

307   22   Cai, Y. *et al.* Experimental and computational framework for a dynamic protein atlas of
308   human cell division. *Nature* **561**, 411–415 (2018).

309   23   Lukinavicius, G. *et al.* SiR-Hoechst is a far-red DNA stain for live-cell nanoscopy. *Nat.*
310   *Commun.* **6**, 8497 (2015).

311   24   Maeshima, K. *et al.* Cell-cycle-dependent dynamics of nuclear pores: pore-free islands and
312   lamins. *J. Cell Sci.* **119**, 4442–4451 (2006).

313   25   Vietri, M. *et al.* Spastin and ESCRT-III coordinate mitotic spindle disassembly and nuclear
314   envelope sealing. *Nature* **522**, 231–235 (2015).

315   26   von Appen, A. *et al.* In situ structural analysis of the human nuclear pore complex. *Nature*
316   **526**, 140–143 (2015).

317   27   Kosinski, J. *et al.* Molecular architecture of the inner ring scaffold of the human nuclear
318   pore complex. *Science* **352**, 363–365 (2016).

319   28   Kim, S. J. *et al.* Integrative structure and functional anatomy of a nuclear pore complex.
320   *Nature* **555**, 475–482 (2018).

321   29   Rout, M. P. & Sali, A. Principles for Integrative Structural Biology Studies. *Cell* **177**,
322   1384–1403 (2019).

13

323   30   Cuylen-Haering, S. *et al.* Chromosome clustering by Ki-67 excludes cytoplasm during

324   nuclear assembly. *Nature*, **587**, 285–290 (2020).

325   31   Onischenko, E. *et al.* Maturation Kinetics of a Multiprotein Complex Revealed by

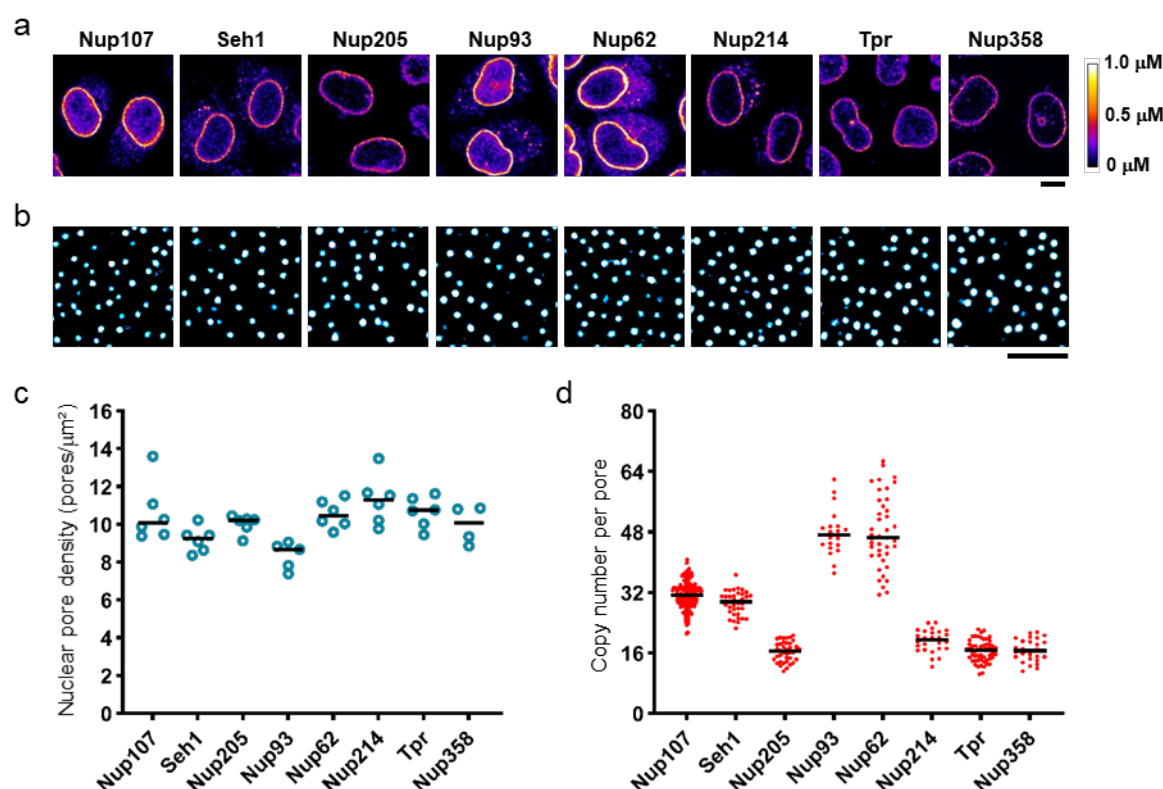326   Metabolic Labeling. *Cell* **183**, 1785–1800 (2020).

Fig. 1 | Quantitative imaging of GFP-knock-in nucleoporin (Nup) cell lines.
a, Genome-edited HeLa cells with homozygously mEGFP-tagged Nups observed by confocal microscopy. Fluorescent intensity was converted into protein concentration by FCS-calibrated imaging[20]. Images were filtered with a median filter (kernel size: 0.25×0.25 μm) for presentation purposes. Scale bar, 10 μm. **b**, **c**, Stimulated emission depletion (STED) microscopy. The genome-edited cells were stained with anti-Nup62 antibody and imaged (**b**), and then the density of nuclear pores was quantified (**c**). The plot is from 6, 6, 6, 5, 6, 6, 6, and 4 cells for Nup107, Seh1, Nup205, Nup93, Nup62, Nup214, Tpr and Nup358, respectively. Scale bar, 1 μm. **d**, Calculated copy number of Nups per nuclear pore. The plot is from 241, 37, 41, 20, 41, 26, 55, and 28 cells for Nup107, Seh1, Nup205, Nup93, Nup62, Nup214, Tpr and Nup358, respectively. The median is depicted as a line.
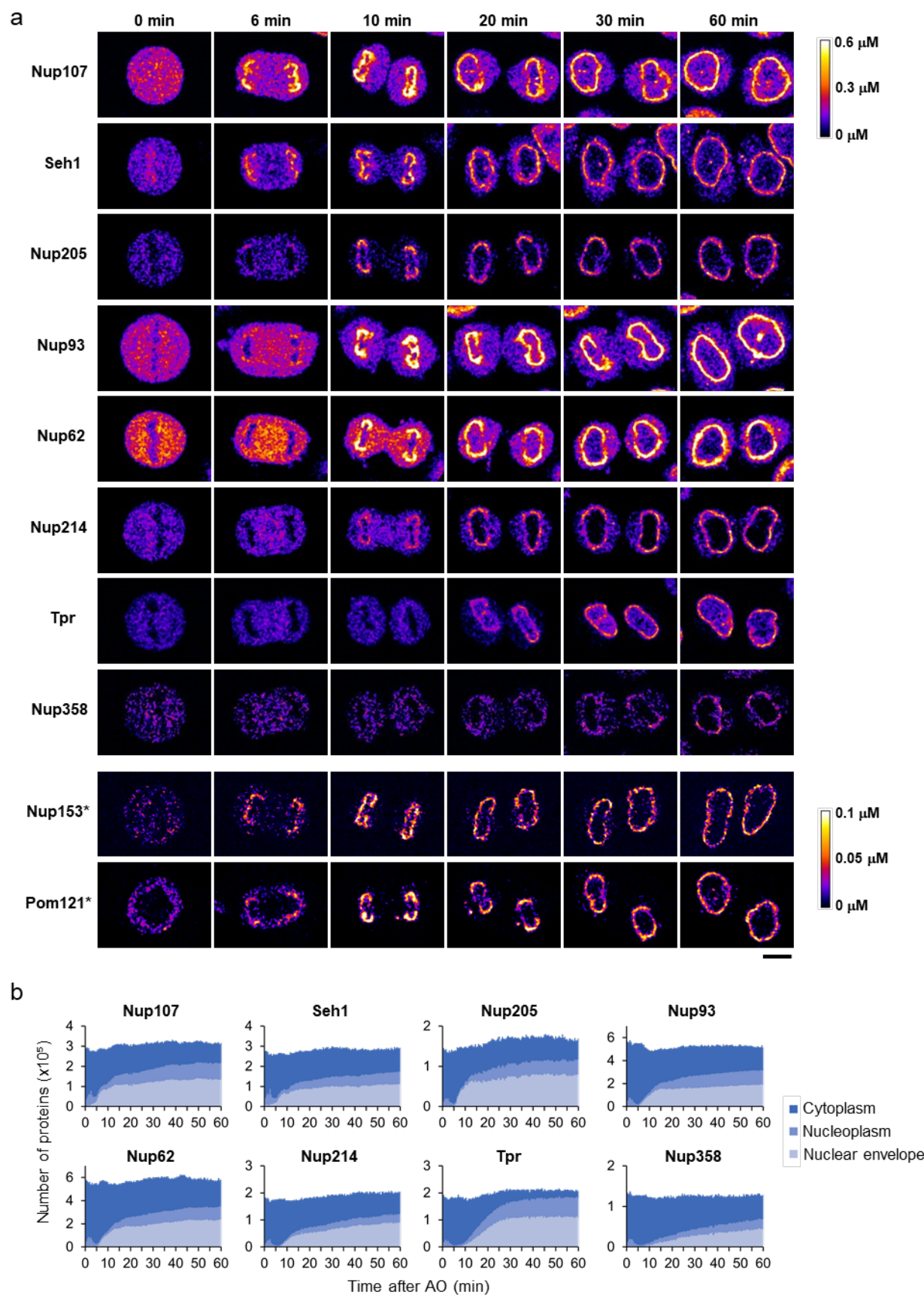
15

341 **Fig. 2 | Dynamic concentration maps of Nups after anaphase onset (AO).**
342 **a**, HeLa cells whose Nups are endogenously tagged with mEGFP or mCherry were imaged every
343 30 sec by three-dimensional confocal microscopy. Single confocal sections are shown. Images
344 were calibrated by FCS to convert fluorescence intensities into cellular protein concentration.
345 *For Nup153 and Pom121, these Nups are not fully validated to be homozygously-tagged.
346 Images were filtered with a median filter (kernel size: 0.25 × 0.25 μm). Scale bar, 10 μm. **b**,
347 Dynamic change of Nup numbers during mitotic exit. The number of Nups in cytoplasm (dark
348 blue), nucleoplasm (medium dark blue) and nuclear envelope (light blue) are plotted against time
349 after anaphase onset. The plot is the mean of 15, 20, 13, 14, 22, 22, 19, and 24 cells for Nup107,
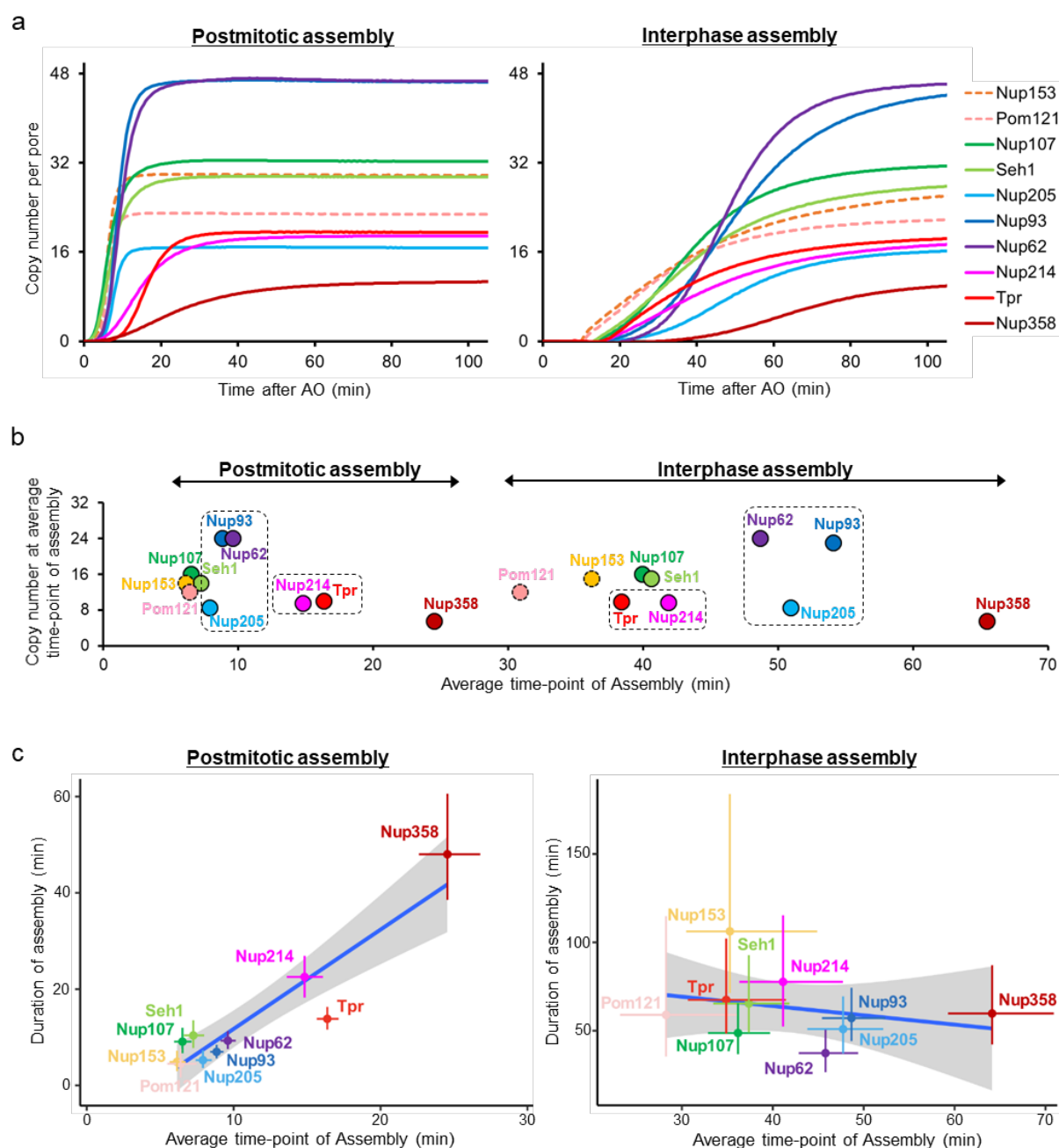350 Seh1, Nup205, Nup93, Nup62, Nup214, Tpr and Nup358, respectively.

17

Fig. 3 | The molecular assembly order and maturation kinetics are distinct for postmitotic and interphase assembly.

a, Plots of the average copy number per nuclear pore computed from mathematical modeling for postmitotic (left) and interphase (right) assembly (see Methods and Extended Data Figs. 2 and 3 for details). For Nup153 and Pom121 (dashed lines), their absolute amount was estimated using the copy number determined from the previous study (32 for Nup153 and 16 for Pom121)[21]. **b**, The average copy number of individual Nups per nuclear pore are plotted along their average time-points of assembly in postmitotic and interphase assembly pathways. **c**, Plots of Nup assembly duration along the time-point of assembly for postmitotic and interphase assembly pathways. The crosses indicate the 95% confidence intervals. The dots are the mean values. Values are listed in Extended Data Table 2. The long straight line shows the result of a linear regression to the mean values. The gray area is the 95% confidence interval of the linear regression.
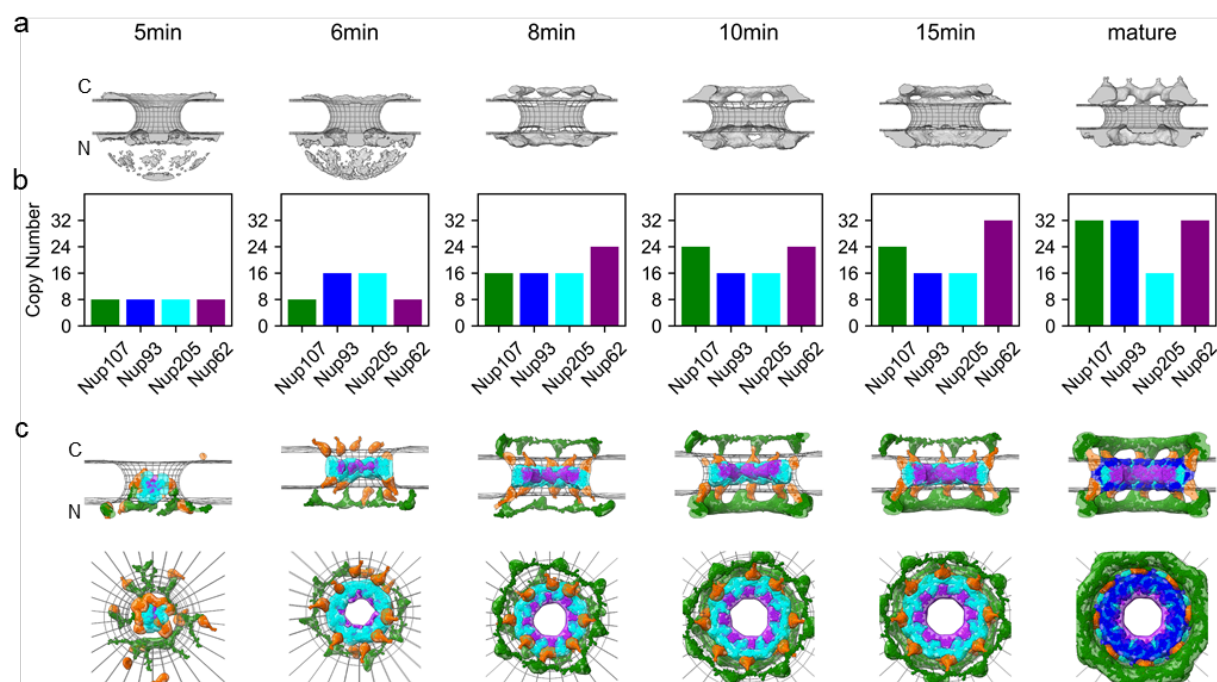
18

Fig. 4 | Integrative model of the postmitotic NPC assembly pathway.
a, Protein density (grey) overlaid with the NE surface (wireframe model, grey) at each time point. C, cytoplasm; N, nucleoplasm. **b**, Copy numbers of Nups used to construct a static NPC model at each time point. **c**, The best-scoring model of postmitotic assembly pathway (top and side views). The uncertainty of each Nup localization is indicated by the density of the corresponding color: Y-complex (green), Nup93-Nup188-Nup155 complex (blue), Nup205-Nup93-Nup155 complex (cyan), Nup62-Nup54 complex (purple), and Nup155 (orange).

373   **Methods**

374   **Cell culture**

375   Wildtype HeLa kyoto cells (RRID: CVCL_1922) were kind gift from Prof. Narumiya in Kyoto

376   University, and the genome was sequenced previously[32]. Cells were grown in high glucose

377   Dulbecco's Modified Eagle's Medium (DMEM) containing 4.5 g/l D-glucose (Sigma Aldrich, St.

378   Louis, MO) supplemented with 10% fetal calf serum (FCS), 2 mM l-glutamine, 1 mM sodium

379   pyruvate, and 100 μg/ml penicillin and streptomycin at 37 °C and 5% CO_2. The mycoplasma

380   contamination was inspected by PCR every 2 or 3 months and was always negative.

381

382   **Genome editing**

383   Monomeric enhanced GFP (mEGFP) and mCherry were inserted into the genome using zinc finger

384   nucleases or CRISPR-Cas9 nickases[17]. The following six cell lines had been generated and

385   published previously: Nup62-mEGFP[33], mEGFP-Nup107[12], mEGFP-Nup205[11], mEGFP-Nup214,

386   mEGFP-Nup358 (also called RanBP2) and Tpr-mEGFP[22]. The following four cell lines were

387   generated in this study: mEGFP-Seh1, Nup93-mEGFP, mEGFP-Nup153, and Pom121-mCherry.

388   The gRNA sequences used for generating these cell lines are summarized in Extended Data Table

389   3. For the Nup93-mEGFP cell line, CRISPR-Cas9 nickases and the donor plasmid were transfected

390   by electroporation (Neon Transfection System, Thermo Fisher Scientific, Waltham, MA) instead

391   of a polymer-mediated transfection reagent.

392

393   **FCS-calibrated live-cell imaging and estimation of Nup copy numbers per NPC**

394   (i) Wild-type cells, (ii) wild-type cells transfected with mEGFP using Fugene6 (Promega,

395   Madison, WI), (iii) mEGFP-Nup107 genome-edited cells, and (iv) the cells of another mEGFP-

396   Nup genome-edited cell line, were seeded on each well of 8-well Lab-Tek Chambered Coverglass

397   (Thermo Fisher Scientific). On the day of live-cell imaging, DMEM was replaced by imaging

398   medium: CO_2-independent medium without phenol red (Invitrogen) containing 20% FCS, 2 mM

399   l-glutamine, and 100 μg/ml penicillin and streptomycin. The imaging medium was supplemented

400   with 50 nM silicon–rhodamine (SiR) Hoechst[23]. Cells were incubated inside the microscope-body-

401   enclosing incubator at 37 °C for at least 30 min before imaging.

402   Calibrated imaging using fluorescence correlation spectroscopy (FCS) was carried out as

403   described in a previous report[20]. Briefly, the confocal volume was determined by performing FCS

404   using a dye with known diffusion coefficient and concentration (Alexa Fluor 488 NHS ester;

405   Thermo Fisher Scientific for mEGFP, Alexa Fluor 568 NHS ester; Thermo Fisher Scientific for

406   mCherry). To convert fluorescence intensity to the concentration, FCS was performed in the cells

407   that transiently-express mEGFP or mCherry alone. Then a calibration curve was obtained by

408   plotting the fluorescence intensity along the concentration. The background fluorescence signal

409   was measured in cells without expressing fluorescent proteins and subtracted.

410   To measure the concentration of Nups, mEGFP-Nup genome-edited cells in interphase were

411   imaged in 3D using a confocal microscope (LSM780; Carl Zeiss, Oberkochen, Germany) and a

412   40× 1.2 NA C-Apochromat water immersion objective (Carl Zeiss) at 37 °C in a microscope-body-

413   enclosing incubator, under the following conditions: 21 optical sections, section thickness of 2.0

414   μm, z-stacks of every 1.0 μm, and the xy pixel size of 0.25 μm. When the NE is not perpendicular

415   to the confocal plane of the 3D stacks, the fluorescence intensity at the NE is nonisotropic in the

416   point-spread function (PSF), which results in underestimation of the signal. To avoid such

417   underestimation, a single plane was selected that contains the largest nuclear area in which the NE

418   is perpendicular to the imaging plane and thus isotropic in the PSF. The fluorescence intensity of

419   Nups was quantified on this single plane using the NE mask with the width of three pixels (0.75

420   μm) that was generated from a SiR-DNA channel. Background fluorescence intensity was

421   measured in wild-type cells without expressing any fluorescent proteins and subtracted. The Nup

422   fluorescence intensity on the NE was converted to the concentration using the calibration curve

423   generated by FCS above. The number of Nups per square micro-meter was calculated from the

424   concentration and then divided by the NPC density per square micro-meter measured by stimulated

425   emission depletion (STED) microscopy. This absolute quantification of Nup copy number with

426   FCS calibration was done using 47 mEGFP-Nup107 genome-edited cells in interphase. For other

427   mEGFP-Nups genome-edited cells, their Nup fluorescent intensities on the NE were directly

428   compared with the ones of mEGFP-Nup107 genome-edited cells on the same 8-well Lab-Tek

429   Chambered Coverglass, and then their concentrations were determined using the intensity ratios

430   to the mean intensity of mEGFP-Nup107 without using a FCS calibration curve. For Pom121-

431   mCherry, the copy number was quantified independently.

432

433   **Measurement of nuclear pore density by stimulated emission depletion (STED) microscopy**

434   For STED super-resolution imaging, cells were fixed with 2.4% formaldehyde (Electron

435   Microscopy Sciences, Hatfield, PA) in PBS for 10 min, extracted with 0.4% Triton X-100 (Sigma

436   Aldrich) in PBS for 5 min, and blocked with 5% normal goat serum (Life Technologies, Carlsbad,

437   CA) in PBS for 10 min at room temperature. Subsequently, the cells were incubated overnight at

438   4°C with a mouse anti-Nup62 (Cat. No. 610497; BD Biosciences, Franklin Lakes, NJ) antibody,

439   and then with an Abberior® STAR RED-conjugated anti-mouse IgG (Cat. No. 2-0002-011-2,

440   Abberior GmbH, Göttingen, Germany) for 30 min at room temperature. After multiple washes in

441   PBS, cells were mounted in Vectashield (Cat. No. H-1500, Vector Laboratories Inc., Burlingame,

442   CA). Super-resolution imaging was performed on a Leica SP8 3X STED microscope as described

443   in a previous report[12]. The images were taken with a final optical pixel size of 20 nm, z-stacks of

444   every 250 nm, and the optical section thickness of 550 nm. Images were filtered with a Gaussian

445   filter (kernel size: 0.5×0.5 pixel) for presentation purposes. The shrinkage of the nucleus by

446   formaldehyde fixation was quantified by comparing the volume of the nuclei of live cells with the

447   ones of fixed cells. The shrinkage was $9.1 \pm 2.6\%$ (the average and standard error, N = 36 cells).

448   The NPC density was corrected for the nuclear shrinkage for the calculation of Nup copy number

449   per NPC in Fig. 1d.

450   To quantify NPC density, the raw STED data were processed in ImageJ

451   (http://rsbweb.nih.gov/ij/) with a mean filter (kernel size: 2 × 2 pixels) and a sliding paraboloid

452   (radius: 5 pixels) for background subtraction. Detection of central peak positions for individual

453   NPCs was carried out with the plugin TrackMate[34], using DoG detector and adjusting the detection

454   threshold as the spot diameter size. The resulting 3D NPC coordinates were used to visualize and

455   determine flat and curved regions of the nucleus. Using this map, circular and ellipsoidal ROIs

456   could then be selected in the flatter parts containing central NPC positions within the Z-depth of

457   approx. 500 nm, which corresponds to 2–3 microscopic slices in the images. The remaining signal

458   outside the ROIs, as in curved regions or cytoplasmic structures were discarded from further

459   analysis. NPC densities were calculated for each cell separately by dividing the number of NPCs

460   within the selected ROIs by the corresponding ROI areas. For each cell line, the values were

461   combined to calculate the mean and median NPC density values.

462

463   **Quantification of Nup copy number in the cytoplasm and the nucleoplasm as well as in non-**

464   **core and core regions of the NE**

465   Mitotic cells were imaged and monitored from anaphase onset for two hours in 3D by confocal

466   microscopy. The microscopy setup and the imaging conditions are described above. Time-lapse

467   imaging for mEGFP-tagged Nups was performed every 30 sec. Photobleaching was negligible and

468   thus not corrected. Time-lapse imaging for Pom121-mCherry was carried out every 60 sec, and

469   photobleaching was corrected by measuring a fluorescence signal decay in a neighboring cell in

470   the same field of view. Visualization of the chromosome surface in 3D was done in the Amira

471   software package[35].

472   To measure the Nup accumulation on the NE, single planes were selected that contain the

473   largest nuclear area at individual time points to avoid underestimation of the signal as mentioned

474   earlier. The Nup intensity was quantified on the NE mask with the width of 0.75 μm that was

475   generated from a SiR-DNA signal at each time point. Except for Nup107 and Seh1, the Nup signal

476   in the cytoplasm and nucleoplasm was measured and used as background. For Nup107 and Seh1,

477   only the cytoplasmic signal was used as background because of their localization at kinetochores.

478   These background values were quantified at individual time points and subtracted from the Nup

479   intensities on the NE. The measured Nup intensity was converted into the concentration and then

480   multiplied with nuclear surface area to calculate the total number of the Nups on the NE. For

481   Nup153 and Pom121, we did not convert the fluorescence intensity to the concentration as the cell

482   lines were not fully validate to be homozygously-tagged.

483   The Nup copy number was also calculated in the cytoplasm and the nucleoplasm during first

484   two hours after anaphase onset. The cytoplasm mask was created by subtracting a mask of the

485   nucleus generated from a SiR-DNA signal from a mask of the whole cell generated from a

486   mEGFP-Nup signal. The mask for the nucleoplasm was created by eroding three pixels of the

487   nuclear mask generated from a SiR-DNA signal. The Nup fluorescence intensity was quantified

488   on these cytoplasmic and nucleoplasmic masks over time and then converted into the

489   concentration. To calculate the total number of Nups in the cytoplasm and the nucleoplasm, the

490   measured concentration was multiplied by the volume of the respective compartments. For the

491   cytoplasm volume, we used the value that was measured previously using fluorescently-labelled

492   dextran[22]. The nucleoplasmic volume was quantified in each mEGFP-Nup knock-in cell line using

493   a SiR-DNA signal as described previously[12].

494   Core regions were predicted on the NE based on a previously described protocol using the

495   core marker Lap-2α[12]. Briefly, nuclear volume was segmented using SiR-DNA fluorescence

496   signals that were processed with a 3D Gaussian filter and a multi-level thresholding. Nuclear

24

497   volume was then divided into inner and outer volumes using the cutting plane that was constructed

498   from the largest eigenvector and the second one orthogonal to the first vector of the pixel

499   coordinates of the nuclear volume. Surface area of each nucleus was calculated and utilized to

500   adjust the size of the inner and outer core regions at individual time points. The previously defined

501   criteria for being core and non-core regions[12] was applied. The position of inner and outer core

502   was determined with respect to the intersection point of the largest eigenvector on the nuclear

503   surface.

504

505   **Mathematical modeling for the nuclear pore assembly kinetics**

506   Previous EM data showed that, within 2 hours after anaphase onset, postmitotic assembly is the

507   dominant process in the non-core region, whereas the slower interphase assembly prevails in the

508   core region[12]. Assuming that this relation is also reflected in the live-cell Nup dynamics, we

509   derived a mathematical model. We assumed that the observed total fluorescence intensity in the

510   non-core, $n(t)$, and core region, $c(t)$, at time-point t after anaphase onset is a linear combination

511   of the postmitotic and interphase assembly processes according to

$$n(\text{t}) = f_N pm(\text{t}) + (1 - f_N) ip(\text{t}) \quad (1)$$

$$c(\text{t}) = f_C\, pm(\text{t}) + (1 - f_C)\, ip(\text{t}), \quad (2)$$

512   where $pm(t)$ and $ip(t)$ are the postmitotic and interphase assembly, respectively. The fraction of

513   postmitotic assembly in the non-core and core regions are denoted f_n and f_c, respectively. To test

514   this assumption and obtain an estimate of the fractions, we used a phenomenological model that

515   accounts for the observed sigmoid-like kinetics

$$pm(t) = \frac{t^{n_p}}{t^{n_p} + K_p^{n_p}}, \qquad \text{for } t \geq d \quad (3)$$

$$ip(t) = \frac{t^{n_i}}{t^{n_i} + K_i^{n_i}}, \qquad \text{for } t \geq d \quad (4)$$

516   and $pm(t < d) = ip(t < d) = 0$. The parameters n_p, K_p and n_i, K_i characterize the postmitotic

517   and interphase kinetics, respectively. The average time-point where a Nup is recruited for the

518   interphase and postmitotic assembly is K_i and K_p, respectively. The parameter d accounts for an

519   additional delay in NPC core region assembly with respect to the non-core region due to the

520   presence of kinetochore microtubule fibers[25]. For the non-core region $d = 0$. For the core region d

521   was estimated from the data.

522   For each assembly mechanisms, we also computed the recruitment duration from Eqs. 3–4.

523   For instance, the time required to recruit 80% of the protein, i.e. from a fraction of $\alpha_1 = 0.1$ up

524   to $\alpha_2 = 0.9$, is given by (see also Extended Data Fig. 4a)

$$\Delta T_p = K_p \left(\left(\frac{\alpha_2}{1 - \alpha_2} \right)^{\frac{1}{n_p}} - \left(\frac{\alpha_1}{1 - \alpha_1} \right)^{\frac{1}{n_p}} \right) \tag{5}$$

$$\Delta T_i = K_i \left(\left(\frac{\alpha_2}{1 - \alpha_2} \right)^{\frac{1}{n_i}} - \left(\frac{\alpha_1}{1 - \alpha_1} \right)^{\frac{1}{n_i}} \right). \tag{6}$$

525   In the model, we subtracted a background computed from the average of the first 3 time points.

526   All data is subsequently normalized to the mean value between 100 and 120 min after anaphase

527   onset. This yields corrected fluorescence intensities, $N(t_j)$ and $C(t_j)$. To find the model

528   parameters we minimized the mean squared distance between data and model for all the time

529   points M

$$\chi^2 = \sum_{j=1}^{M} \left(\left(\frac{N(t_j) - n(t_j)}{\sigma_N(t_j)} \right)^2 + \left(\frac{C(t_j) - c(t_j)}{\sigma_C(t_j)} \right)^2 \right), \tag{7}$$

530   where $\sigma_N(t_j)$ and $\sigma_C(t_j)$ are the respective standard deviation in the non-core and core region.

531   The parameter estimation has been performed in two steps. First, for each protein/cell-line,

532   we estimated the postmitotic fraction in the core and non-core region and the kinetic parameters.

533   All in all we computed 60 parameters (6 parameters per protein) from 4446 data points. We found

534   that the model well agrees with the data (Extended Data Figs. 2 and 3, $R^2 > 0.99$). For the

26

535 postmitotic fractions, we obtained on average $f_n = 0.857$ [0.76, 0.95] and $f_c = 0.295$ [0.17, 0.4],

536 where the number in brackets indicates the 95% confidence interval as estimated using the profile

537 likelihood method[36]. Importantly, the obtained postmitotic fractions are well in agreement with

538 the previously reported estimates obtained from EM-data[12]. The delay in pore formation between

539 core and non-core region was estimated by systematically varying d from 0 to 6 min in steps of 1

540 minute. A value of $d = 2$ min, gave optimal result. In a second step we used the previously

541 estimated average postmitotic fractions and d and recomputed the kinetics parameters for each

542 protein. The model with reduced parameters gave very similar results. To verify if the choice of

543 common postmitotic fractions for all Nups is valid, we computed the Baysian information criterion

544 (BIC) according to the previous report[37]. The difference in BIC between the model with reduced

545 parameters, 42 parameters for all proteins, compared to the full model, 60 parameters, was -7,

546 indicating that the model with reduced parameters is justified. The obtained parameter values are

547 listed in Extended Data Table 2.

548   Our validated model can be used to derive the underlying post-mitotic and interphase

549 assembly kinetics. Using Eqs. 1–2 we obtain

$$ip(t) = \frac{f_n c(t) - f_c n(t)}{f_n - f_c}. \tag{8}$$

$$pm(t) = \frac{(1 - f_c)n(t) - (1 - f_n)c(t)}{f_n - f_c}. \tag{9}$$

550 These equations can directly be applied to the experimental data $N(t)$ and $C(t)$ using the previously

551 estimated fraction f_n and f_c.

552   In Fig. 3c we see a strong positive correlation for the average time point of assembly and the

553 duration of assembly. One can prove that such a relation is expected for an irreversible sequential

554 assembly mechanism with linear rate constants. Using the definition for average time and

555 duration[38], the average time-point of a protein binding at step i is

$$\tau_i = \sum_{j=1}^{i} 1/k_j, \tag{10}$$

556 where k_j is the binding rate constant of a protein binding at step j to the complex. The duration of

557 assembly of a protein binding at step i is given by

$$\theta_i = 2\sqrt{\sum_{j=1}^{i} 1/k_j^2}. \tag{11}$$

558 From Eqs 10–11, it is clear that $\tau_{i+1} > \tau_i$ and $\theta_{i+1} > \theta_i$ for any parameter combinations.

559 Therefore, late binding proteins show a longer duration of assembly.

560

561 **Structural modeling of NPC assembly pathway**

562 A model of the assembly pathway is defined by a series of static structures, including a static

563 structure at each sampled time point along the assembly process. Therefore, we model the NPC

564 assembly by first modeling static structures at each time point, independently from each other. We

565 then enumerate alternative assembly pathways and rank them based on the static structure scores

566 and plausibility of transitions between successive static structures.

567 *Integrative modeling of static structures at each time point*

568 The static structures are modeled by standard integrative structure modeling[29], as follows.

569 *Representing a static structure model*

570 The time points correspond to times with available ET protein densities[11]: 5min, 6 min, 8 min, 10

571 mins, and 15 min after anaphase onset. We divide the mature NPC structure (PDB 5a9q, 5ijo) into

572 eight spokes and further divide each spoke into a set of rigid subcomplexes, including the Y-

573 complex, the inner ring Nup205-Nup155-Nup93 subcomplex, the inner ring Nup93-Nup188-

574 Nup155 subcomplex, and the central channel Nup62-Nup58-Nup54 subcomplex. For each

575 domain, we coarse-grained the structure by grouping 10 consecutive amino acid residues into a

576 single bead at the center of mass of those residues. Each subcomplex is represented as a rigid body.

28

577   The NE is represented as a fixed toroid surface embedded in two parallel planes. Thus, the

578   variables of the model include the Euclidean coordinates of the Nup subcomplexes and the copy

579   number of each Nup subcomplex.

580   We set the inner pore diameter and minor radius of the pore at each time point to the mean of

581   previously determined NE cross sections[11] with a pore diameter of 51.5 nm, 58.4 nm, 72.7 nm,

582   84.6 nm, 79.8 nm, and 87 nm; and minor radius of 21.4 nm, 21.2 nm, 21.5, 20.3 nm, 17.1 nm and

583   15 nm for time points at 5min, 6min, 8min, 10min, 15min, and the mature pore, respectively.

584   *Scoring a static structure model*

585   The copy numbers of the NPC subcomplexes at each time point were restrained by a Gaussian

586   function with mean and variance determined by the single-cell traces presented in this study. The

587   relative likelihood of a set of copy numbers is proportional to the product of individual Gaussian

588   likelihoods.

589   Distances between pairs of Nups that are in contact with each other in the native NPC

590   structure[26,27] were restrained by a harmonic Gō-like model[39]. Inter-subcomplex contacts within 5

591   nm in the mature structure were restrained by a harmonic function (strength 0.01 kcal/mol Å).

592   Each Gō-like scoring term was scaled at each time point, from zero at the first time point to full

593   strength at the mature pore time point. Distances between all pairs of Nups were also restrained

594   by a harmonic excluded volume restraint (strength 0.01 kcal/mol Å). Proximity between Nup

595   domains containing a membrane interacting ALPS-motif and the NE was restrained by a harmonic

596   term (strength 0.1 kcal/mol Å), based on their sequences. Overlap between the Nups and NE

597   surface was avoided by imposing a harmonic repulsion between the Nups and NE surface (strength

598   of 0.01 kcal/mol Å).

599   The shape of a static structure was restrained by a correlation coefficient between the model

600   and ET protein density[11]. The forward model density was represented by fitting each Nup

601   subcomplex with a Gaussian mixture model of two components per subcomplex copy using the

29

602　　*gmconvert* utility[40]. Similarly, the ET protein densities at each time point were represented with a

603　　Gaussian mixture model with 150 components fit to the experimental density.

604　　*Sampling static structure models*

605　　A state of the NPC at any given time point is defined by the copy numbers and coordinates of its

606　　components. Only copy number assignments and structures consistent with the C-8 symmetries

607　　were sampled. In addition, we only sampled structures for the top 20-scoring Nup copy number

608　　combinations. Each sampling started with the mature pore structure, followed by applying 10^6

609　　Monte Carlo moves. These moves included rotational and translational perturbations to each Nup

610　　subcomplex, drawn from a uniform distribution in the range from -0.04 to +0.04 radians and from

611　　-4 to +4 Å, respectively.

612　　*Modeling the assembly pathway*

613　　With the static structure models in hand, we connect them into complete alternative assembly

614　　pathways, as follows.

615　　　　Each pathway is represented by a static structure at each sampled time point, starting with t =

616　　5 min and culminating in the native structure; we do not model the completely disassembled NPC.

617　　The score of a pathway is the sum of the scores for the static structures on the pathway (defined

618　　above) and transitions between them. A transition score is uniform for all allowed transitions. A

619　　transition between two successive static structures is allowed if the subcomplexes in the first

620　　structure are included in the second structure. All possible pathways were enumerated, scored, and

621　　ranked. The best-scoring pathways were extracted for further analysis (Fig. 4).

622

623　　**Sample size determination and statistical analysis**

624　　For quantitative imaging in Fig. 1a, d, the data were from 4, 4, 4, 2, 3, 2, 3, and 2 independent

625　　experiments for Nup107, Seh1, Nup205, Nup93, Nup62, Nup214, Tpr and Nup358, respectively.

626　　STED imaging in Fig. 1b, c was from one independent experiment. For dynamic quantitative

627   imaging in Fig. 2, the data were from 4, 4, 4, 2, 3, 4, 3, 2, 2, and 4 independent experiments for

628   Nup107, Seh1, Nup205, Nup93, Nup62, Nup214, Tpr, Nup358, Nup153, and Pom121,

629   respectively. Statistical analyses were performed only after all the data were taken. Sample sizes

630   for each experiment are indicated in figure legends. Sample sizes were based on pilot experiments

631   to determine the number of cells required to observe stable population averages with high

632   Pearson's correlation between replicates. Videos of dividing cells with rotating nuclei are removed

633   from the analysis, because we cannot properly assign the non-core and core regions.

634

635   **Data and code availability**

636   Fluorescence images will be available in the Image Data Resource (IDR;

637   https://idr.openmicroscopy.org/) or the BioImage Archive

638   (https://www.ebi.ac.uk/biostudies/BioImages/studies). Our integrative spatiotemporal model of

639   the postmitotic assembly of the human NPC is available in PDB-Dev (https://pdb-

640   dev.wwpdb.org/) under the accession code XX (PDB submission in progress). Integrative

641   Modeling Platform (IMP) is an open source program freely available under the LGPL license at

642   http://integrativemodeling.org; all input files, scripts, and output files are available at

643   http://integrativemodeling.org/npcassembly.

644

645   **Method references**

646   32   Landry, J. J. *et al.* The genomic and transcriptomic landscape of a HeLa cell line. *G3*

647   *(Bethesda)* **3**, 1213–1224 (2013).

648   33   Farrants, H. *et al.* Chemogenetic Control of Nanobodies. *Nat. Methods* **17**, 279–282

649   (2020).

650   34   Tinevez, J. Y. *et al.* TrackMate: An open and extensible platform for single-particle

651   tracking. *Methods* **115**, 80–90 (2017).

652   35   Pruggnaller, S., Mayr, M. & Frangakis, A. S. A visualization and segmentation toolbox for

653   electron microscopy. *J. Struct. Biol.* **164**, 161–165 (2008).

654   36   Raue, A. *et al.* Structural and practical identifiability analysis of partially observed

655   dynamical models by exploiting the profile likelihood. *Bioinformatics* **25**, 1923–1929

656   (2009).

657   37   Kass, R.E. & Raftery, A. E. Bayes Factors. *J. Am. Stat. Assoc.* **90**, 773–795 (1995).

658   38   Heinrich, R., Neel, B. G., & Rapoport, T. A. Mathematical models of protein kinase signal

659   transduction. *Mol. Cell* **9**, 957-70 (2002).

660   39   Go, N. & Abe, H. Noninteracting local-structure model of folding and unfolding transition

661   in globular proteins. I. Formulation. *Biopolymers* **20**, 991–1011 (1981).

662   40   Kawabata, T. Gaussian-input Gaussian mixture model for representing density maps and

663   atomic models. *J. Struct. Biol.* **203**, 1–16 (2018).

664

Acknowledgments

675

Author contributions

677 SO, JOBT, AS, and JE designed the project. SO performed all the fluorescence microscopy

678 experiments and analyses. JOBT performed integrated structural modeling. AZP carried out

679 mathematical modeling for the nuclear pore assembly kinetics. AR developed an analysis pipeline

680 for nuclear pore density measurement. MJH established a computational image analysis pipeline

681 to quantify fluorescence intensities in non-core and core regions in 3D time-lapse images. M.K.,

682 A.C. and B.K. generated genome-edited cell lines. AS and JE supervised the work. SO, JOBT,

683 AS, and JE wrote the paper. All authors contributed to the analysis and interpretation of data and

684 provided input on the manuscript.

685

686 **Competing interest declaration**

687 The authors declare no competing interests.

688

689 **Additional information**

690 The manuscript contains supplementary material (Extended Data Figs. 1 to 4 and Extended Data

691 Tables 1 to 3).